

How do convective cold pools influence the atmospheric boundary layer near two wind turbines in northern Germany?

Jeffrey D. Thayer¹, Gerard Kilroy¹, and Norman Wildmann¹

¹German Aerospace Center (DLR), Institute for Atmospheric Physics, Oberpfaffenhofen, Germany

Correspondence: Jeffrey D. Thayer (jeffrey.thayer@dlr.de)

Abstract. With increasing wind energy in the German energy grid, it is crucial to better understand how particular atmospheric phenomena can impact wind turbines and the surrounding atmospheric boundary layer. Deep convection is one source of uncertainty for wind energy prediction, with the near-surface convective outflow (i.e., cold pool) causing rapid kinematic and thermodynamic changes that are not adequately captured by operational weather models. Using 1-minute meteorological mast and remote-sensing vertical profile observations from the WiValdi research wind park in northern Germany, we detect and characterize 120 convective cold pool passages over a period of 4 years in terms of their temporal evolution and vertical structure. We particularly focus on variations in wind-energy-relevant variables (wind speed and direction, turbulence strength, shear, veer and static stability) within the turbine rotor layer (34-150 m height) to isolate cold pool impacts that are critical for wind turbine operations. Near hub-height (92 m) during the gust front passage, there are relatively increased wind speeds up to +4 m s⁻¹ in addition to the background flow, a relative wind direction shift up to +15°, and increased turbulence strength for a median cold pool. Given hub-height wind speeds lying within the partial load region of the power curve for the detected cases, there is an increase in estimated power of up to 50% which lasts for 30 minutes. We find a 'nose shape' in relative wind speeds and virtual potential temperature (θ_v) at hub-height during gust front passages, with larger wind direction changes closer to the surface. This manifests as asymmetric fluctuations in positive shear, negative veer, and static stability across the rotor layer, with relative variations below hub-height at least twice as large compared with above hub-height and temporarily opposite signs for stability that have complex implications for turbine wakes. Doppler wind lidar profiles indicate that kinematic changes associated with the gust front extend to a height of 700-800 m, providing an estimate for cold pool depth and highlighting that cold pool impacts would typically extend beyond the height of current onshore wind turbines. After the cold pool gust front passage, there is gradually increasing static stability, with a median decrease in near-surface θ_v of -2.7 K, a gradual decrease in hub-height turbulence strength, and faster recovery of wind speed than wind direction.

1 Introduction

With the share of wind energy in the German power grid increasing from 1.7% in 2000 to 34% over the first half of 2024 (BMWK, 2024; Fraunhofer ISE, 2024), the density of wind turbines across Germany is increasing. This indicates that smaller-scale phenomena can impact a greater number of wind turbines, and that the German energy sector is becoming more susceptible to shorter-duration power fluctuations. The stability and balancing of the German electrical grid operates on lead

times down to 5 minutes, which increases the utility of minute-scale wind power forecasting for energy trading and wind turbine control (Wurth *et al.*, 2019). Despite the identified importance of short-term wind power forecasting, there are continuing uncertainties with power forecasts. The median annual wind energy production still tends to be overpredicted globally, with uncertainties of $\sim 6\%$ (Lee and Fields, 2021). Over Germany, larger day-ahead power forecast errors have been associated with various meteorological events, with a 1-3% installed capacity day-ahead forecast error in any given month indicating a wide-range of meteorological causes possibly affecting the forecasting errors (Steiner *et al.*, 2017). Meteorological impacts on power production are therefore one noteworthy consideration for limiting the power prediction uncertainty, with reductions in wind speed (U) uncertainty having an out-sized improvement on predicted power (P) since $P \sim U^3$ (Lee and Fields, 2021). As such, improving understanding of short-term low-level wind speed variations associated with meteorological events is crucial for reducing short-term wind power forecasting uncertainties.

Rapid changes in the wind profile over the lowest few hundred meters of the atmospheric boundary layer (ABL) on timescales ranging from a few minutes to a few hours (e.g., wind ramps) are an important driver of variations in wind power. Wind ramps can be produced by a range of meteorological phenomena, including mid-latitude cyclones, low-level jets, sea breezes, and deep convection, and therefore wind ramps can occur across a range of timescales and spatial scales (Gallego-Castillo *et al.*, 2015). Past work on wind ramps over Europe has largely focused on the turbine impacts without providing a detailed verification of the meteorological cause of the wind ramps (Vincent *et al.*, 2011; Kelly *et al.*, 2021; Lochmann *et al.*, 2023). When meteorological causes of wind ramps have been identified, the focus was on synoptic-scale weather phenomena (Valdecabres *et al.*, 2020) or specifically mid-latitude cyclones (Steiner *et al.*, 2017). Steiner *et al.* (2017) additionally found that 18% of analyzed wind ramps could be related to convective systems or unresolved downward mixing, but this wind ramp category was not investigated in detail and deeper evaluation would have been limited by the ~ 7 km horizontal resolution of the numerical weather prediction (NWP) model used in their study. Beyond this 'convective systems' wind ramp category broadly outlined in Steiner *et al.* (2017), we are not aware of additional work concerning wind power fluctuations induced by convective wind ramps over Europe.

In this regard, quantification of short-term thunderstorm impacts using wind energy-relevant variables, and specifically related to thunderstorm near-surface outflow, has rarely been performed. For example, Lombardo *et al.* (2014), Gunter and Schroeder (2015), and Canepa *et al.* (2020) each analyzed strong thunderstorm outflow events (i.e., downbursts) using wind energy-relevant variables with a limited sample size (10 or fewer), but did not investigate a larger sample of cases or the broader range of thunderstorm outflow intensities that can occur. Mature-stage deep convection produces a precipitation-induced downdraft with descending cold air that spreads outward once reaching the surface (Byers and Braham, 1948). This 'cold pool' has a low-level outflow boundary at its periphery known as a gust front, which is typically characterized by increased horizontal wind speeds, a wind direction shift, and increased turbulence relative to the background environment (Benjamin, 1968; Goff, 1976; Wakimoto, 1982; Droegemeier and Wilhelmson, 1987). As thunderstorm gust front winds tend to maximize within the height range of the turbine rotor layer (Lombardo *et al.*, 2014; Gunter and Schroeder, 2015; Canepa *et al.*, 2020) and thunderstorm ramp-up events typically occur on timescales from 1-5 minutes (Lombardo *et al.*, 2014), gust fronts are simultaneously crucial for assessing short-term wind turbine-related impacts and under-resolved by NWP models both spatially

and temporally. This limitation is potentially exacerbated by the fact that NWP models tend to underestimate extreme winds due to mesoscale smoothing, with this effect especially pronounced on the sub-hourly timescale (Larsen *et al.*, 2012). High-frequency kinematic observations encompassing the turbine rotor layer are thus a promising tool for accurately characterizing rapid variations in wind power caused by convective cold pools and their associated gust fronts.

65 The gust front is not the only aspect of convective cold pools relevant to wind energy applications. Near-surface thermal stability changes in the ABL, such as those that occur after a cold pool gust front passage, also have notable implications for variations in wind turbine power generation. A convective (stable) boundary layer is associated with higher (lower) turbulence (Stull, 1988), which contributes to the amount of turbulent mixing in the wind turbine wake region. Decreased wind speed deficits (i.e., faster wake recovery and shorter wake length) and greater turbulence downstream of wind turbines occur in
70 convective conditions compared with a neutral boundary layer (Zhang *et al.*, 2013; Iungo and Porte-Agel, 2014; Abkar and Porte-Agel, 2014), generally leading to decreased power deficits for wind farms depending on turbine spacing (Hansen *et al.*, 2012). In short, the ABL stability affects the turbulence strength, which then influences how quickly the turbine wake recovers (Wildmann *et al.*, 2018) and whether the turbine wake impacts power generation of downstream turbines. With short-term increases in turbulence accompanying the cold pool gust front (e.g., Droegemeier and Wilhelmson, 1987; Lombardo *et al.*,
75 2014; Canepa *et al.*, 2020) and short-term increases in near-surface stability occurring within the cold pool interior, passages of convective cold pools over wind turbines provide a unique opportunity to examine the complex interactions between ABL stability regimes and wind power production.

With a particular focus on convective cold pool impacts within the turbine rotor layer, we investigate short-term kinematic and thermodynamic variations near two utility-scale wind turbines within the WiValdi research wind farm¹ in northern
80 Germany from 2020-2024. The flat terrain and vast array of in-situ and remote sensing instrumentation available at this research site provide a unique opportunity for isolating and characterizing convective cold pool impacts relevant for wind energy. We extend the WiValdi climatological work of Wildmann *et al.* (2022) by highlighting thunderstorm-related environmental effects, with this region of northern Germany notably having a relatively high frequency of convective cells (Wilhelm *et al.*, 2023) and density of wind turbines (Bouchard and Romanic, 2023). Given the 1-5 minute timescale of thunderstorm ramp-up
85 events and the importance of minute-scale forecasting for the German wind power sector, we utilize high-frequency (1-minute) measurements from meteorological mast, Doppler wind lidar velocity azimuth display (VAD) scans (Wildmann *et al.*, 2020), and microwave radiometer instrumentation at WiValdi to analyze the near-surface environmental changes associated with cold pools. Radar composite datasets from the German Meteorological Service (DWD) provide verification of the parent convective cells. Using summertime cold pool studies focused on the Netherlands (Kruse *et al.*, 2022) and northern Germany (Kirsch *et al.*, 2021; 2024) as a foundation, we examine year-round cold pool events with particular emphasis on wind-energy-relevant
90 variables. The primary research questions guiding this work are as follows:

- How much does the wind speed, wind direction, and temperature change in the ABL during observed convective cold pool passages near the WiValdi wind turbines?

¹More information can be found on the official WiValdi wind park website (www.windenergy-researchfarm.com).

- To what extent do wind-energy-relevant variables (wind speed and direction, turbulence strength, wind shear, wind veer, static stability) change throughout the turbine rotor layer during these convective cold pool passages?
- Is there a significant variation in estimated wind power production at turbine hub-height during these convective cold pool passages?

Section 2 outlines our observational datasets, instrumentation, and cold pool detection methodology. Sections 3 and 4 describe the temporal evolution and vertical structure of cold pool characteristics, respectively. Section 5 highlights changes throughout the turbine rotor layer and estimates of wind power increase during cold pool passages. Section 6 contains a summary of our findings along with the conclusions for this study.

2 Data and Methodology

2.1 WiValdi instrumentation

The WiValdi research wind farm operated by the German Aerospace Center (DLR) in Krümmendeich, Germany is located in coastal flatlands near the mouth of the River Elbe by the North Sea (Fig. 1a). This large-scale research facility contains two 4.2-MW Enercon E-115 wind turbines (Fig. 1b) that have hub heights of 92 m and rotor diameter D of 116 m, are separated by approximately 500 m (i.e., 4.3 rotor blade diameters = 4.3 D), and are aligned along the primary west-southwesterly wind direction (Wildmann *et al.*, 2024). One 150-m meteorological mast located 2 D in front of the westernmost turbine (i.e., T1) provides inflow conditions at multiple heights throughout the turbine rotor layer (see Table 1). On this 'inflow mast', ultrasonic anemometers (hereafter, sonic) lie at heights of 34 m, 62 m, 85 m, 120 m, and 149 m, while temperature and relative humidity sensors are located at 34 m, 62 m, 85 m, 120 m, and 143 m. Barometers are only located at 10 m and 85 m, so pressure values at other heights are obtained via the hypsometric equation starting at 10 m. Using 1-minute averaged measurements, the inflow meteorological mast observations, which are available starting from 14 November 2022, will be used in this study to validate the remote sensing vertical profiles and characterize the convective cold pool impacts within the rotor layer (i.e., 34-150 m). As a measure for turbulence, 1-minute turbulent kinetic energy (TKE) dissipation rate ε is calculated from the second-order structure function according to Bodini *et al.* (2019) using the 85-m sonic anemometer observations that have a temporal frequency of 20 Hz. We use this variable to characterize turbulence strength since it can be calculated for short time periods and can thus provide information about rapid changes during gust front passages.

Vertical profiles of wind speed and direction are provided by a Leosphere WindCube 200S pulsed Doppler wind lidar that was installed on 4 November 2020 approximately 400 m to the east of the easternmost turbine (i.e., T2). This lidar has a pulse length of 200 ns, a measurement range for radial velocities between -30 to 30 m s⁻¹, and a minimum observing line-of-sight distance of 100 m (two times the minimum range gate length). Radial velocity retrievals from a Doppler wind lidar are more greatly attenuated by precipitation and low cloud cover (e.g., fog).

This lidar has the capability to perform horizontal plan-position indicator (PPI) scans, vertical range-height indicator scans, and fixed direction scans. A sub-category of PPIs are conical scans at a constant elevation angle, known as Velocity-

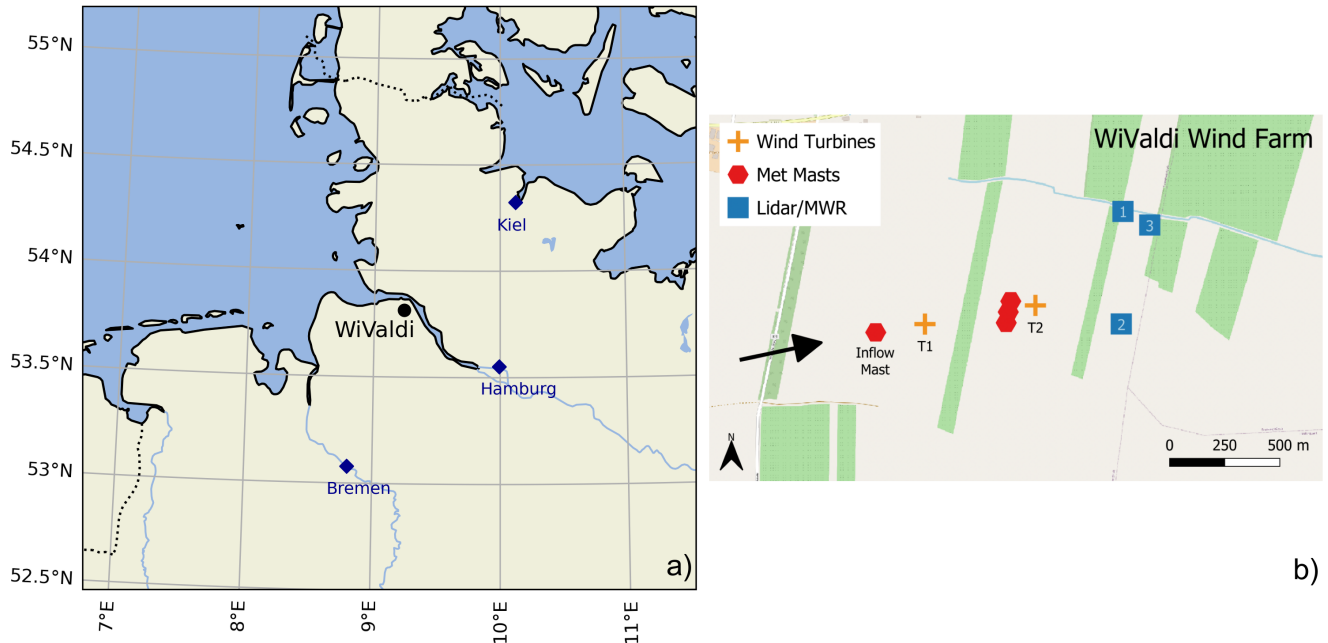


Figure 1. (a) Map of northern Germany centered on the location of the WiValdi wind farm. Blue diamonds indicate nearby major cities, while dashed lines indicate country borders. (b) Detailed layout of WiValdi, indicating the locations of the wind turbines, meteorological masts, MWR, lidar, and underlying simple terrain. The blue squares represent the location of both the Lidar and MWR, with the overlaid numbers indicating their different positions in chronological order: November 2020 - March 2022 (1), October 2022 - May 2024 (2), and May 2024 - present (3). Black arrow indicates the primary west-southwesterly wind direction at WiValdi. Background map: ©OpenStreetMap contributors 2025. Distributed under the Open Data Commons Open Database License (ODbL) v1.0.

Azimuth Display (VAD) scans, which allow for determinations of the horizontal wind components using the so-called VAD technique. We perform VAD scans at two different elevation angles: 35.3° and 75° . The 75° VAD scan (VAD75) has a higher vertical range and a smaller horizontal footprint, whereas the 35.3° scan (VAD35) can be used to determine TKE (Kropfli, 1986; Wildmann *et al.*, 2020). In both cases, an averaged profile of the 3D wind vector is measured horizontally across the cone at each range gate (i.e., every height), with a complete scan lasting ~ 72 s. Each VAD scanning pattern is run for 30 minutes every hour, with 25 scans per elevation angle. Given a minimum measurement height of 57 m and 96 m for the VAD35 and VAD75 scans respectively, we obtain ‘hub-height’ lidar winds at 100 m to have consistent coverage during both scanning patterns. Lidar data is linearly interpolated to 1-minute temporal resolution throughout the vertical profile to capture rapid wind variations associated with convective cold pools, but we limit interpolation to within surrounding reliable measurements (signal-to-noise ratio from 0 to -25) and do not interpolate across more than 1 missing value.

Adjacent to the lidar, there is a passive HATPRO G5 microwave radiometer (MWR; Rose *et al.*, 2005) manufactured by Radiometer Physics GmbH that was installed on 26 November 2020 and which provides vertical profiles of temperature and

| Measurement System | Instrument Type | Measured Variable | Measurement Height(s) | Measurement Time Period | Measurement Temporal Resolution(s) |
|--|--|-------------------|---------------------------------------|--|------------------------------------|
| Wind Turbines | Enercon E-115 | Power Generation | 92 m (Hub height) | 23 May 2024 - 30 November 2024 | 100 Hz |
| Inflow Meteorological Mast | Ultrasonic anemometer (i.e., sonic) | Wind Speed | 85 m | 19 October 2022 - 30 November 2024 | 20 Hz |
| | | | 34, 62, 120, 149 m | 1 April 2023 - 30 June 2024 | 10 Hz |
| | | Wind Direction | 85 m | 19 October 2022 - 30 November 2024 | 20 Hz |
| | | | 34, 62, 120, 149 m | 1 April 2023 - 30 June 2024 | 10 Hz |
| | Hygro-Thermometer | Temperature | 85 m | 19 October 2022 - 30 November 2024 | 20 Hz |
| | | | 34, 62, 120, 143 m | 1 April 2023 - 30 June 2024 | 10 Hz |
| | | Relative Humidity | 85 m | 19 October 2022 - 30 November 2024 | 20 Hz |
| | | | 34, 62, 120, 143 m | 1 April 2023 - 30 June 2024 | 10 Hz |
| | Barometer | Pressure | 85 m | 19 October 2022 - 30 November 2024 | 20 Hz |
| | 10 m | | 1 April 2023 - 30 June 2024 | 10 Hz | |
| Rain gauge | Rainfall | 8 m | 19 October 2022 - 30 November 2024 | 1 minute | |
| Doppler Wind Lidar (i.e., Lidar) | WindCube 200S [Leosphere] | Wind Speed | 100 - 1000 m (25 m increments) | 04 November 2020 - 30 November 2024 | 72 seconds |
| | | Wind Direction | 100 - 1000 m (25 m increments) | | |
| Microwave Radiometer (i.e., MWR; adjacent to Lidar) | HATPRO G5 [Radiometer Physics] | Temperature | 0, 10, 25, 50, 75, 100 m | 26 November 2020 - 30 November 2024 | 1 minute |
| | | Relative Humidity | 0, 10, 25, 50, 75, 100 m | | 1 minute |
| Ground Weather Station (attached to MWR) | Ultrasonic anemometer (i.e., sonic) | Wind Speed | 2 m | 26 November 2020 - 30 November 2024 | 10 seconds |
| | | Wind Direction | 2 m | | 10 seconds |
| | Thermometer | Temperature | 2 m | | 10 seconds |
| | Hygrometer | Relative Humidity | 2 m | | 10 seconds |
| | Barometer | Pressure | 2 m | | 10 seconds |
| | Rain gauge | Rainfall | 2 m | | 10 seconds |

Table 1. Summary of WiValdi instrumentation, measurement heights, and time periods used in this study. Measurement temporal resolution reflects the native output frequency of each instrument, while 1-minute averaged data is used throughout our analyses unless otherwise indicated.

140 humidity. We note that the lidar and MWR were slightly moved within the wind park every couple of years (Fig. 1b, blue squares), but were moved on the same days, kept adjacent to each other, and remained east of the T2 turbine by approximately the same distance. With an associated ground weather station for obtaining surface environmental conditions, an MWR passively retrieves vertical profiles through usage of multiple brightness temperature measurements within the oxygen and water vapor absorption bands. Absolute calibration using liquid nitrogen is performed about every half year, with a gain calibration using the internal hot target being carried out every 30 minutes and noise calibration is automatically performed internally with high frequency during normal operations.

145 The HATPRO G5 MWR can perform zenith and boundary-layer scans to obtain temperature profiles, while humidity profiles are determined only from the zenith scans. Zenith scans point directly upwards and retrieve measurements up to 10 km altitude, with a general decrease in spatial resolution with increasing height (especially above 2 km). Boundary-layer scans are performed at 10 different elevation angles ranging from 4-90° up to 1.2 km altitude towards the south (185° azimuth), which can more accurately capture vertical gradients in temperature and humidity than zenith scans. The MWR at WiValdi performs a
150 boundary-layer scan lasting about 100 seconds every ten minutes. Otherwise, the instrument measures at zenith (90° elevation) to obtain 1-minute temperature and humidity. To better capture rapid environmental variations associated with convective cold pool passages, we use the 1-minute zenith vertical profile data for this study.

2.2 Cold pool detection algorithm

Following guidance from recent European cold pool studies (Kirsch *et al.*, 2021; Kruse *et al.*, 2022; Kirsch *et al.*, 2024),
155 we identify convective cold pools at WiValdi using 1-minute time series data. High-frequency observations on the minute-scale are crucial for capturing the rapid environmental changes associated with cold pools, while near-surface observations ensure identification of the cold pool thermodynamical signal which is strongest near the surface (e.g., Barnes and Garstang, 1982; Kirsch *et al.*, 2021). Using 2-m in-situ measurements from the ground weather station attached to the MWR across 4 years (26 November 2020 - 30 November 2024), we detect cold pool passages throughout the year using the following procedure:

- 160 • Smooth the 2-m virtual potential temperature (θ_v) time series using 11-minute rolling averages, following Kruse *et al.* (2022) which extends the methodology of de Szoeké *et al.* (2017). This smoothing reduces the effect that random θ_v fluctuations could have on misidentifying the starting time of a cold pool passage, while θ_v rather than temperature is used to account for pressure and moisture variations.
- Isolate time periods of *continuous* 2-m θ_v decreases to further minimize misidentification caused by random θ_v fluctuations, and which follows from observed cold pool horizontal structure where temperature decreases approximately
165 linearly from the edge to the center (Kirsch *et al.*, 2024).
- Identify the time step when the smoothed 2-m θ_v continuously decreases by at least 0.5 K as ' T_0 ', following Kirsch *et al.* (2021).
- Continuous- θ_v -decrease time periods include at least one time step of measurable rainfall exceeding 1 mm hr⁻¹ and a
170 positive wind speed anomaly relative to the daily mean wind speed within +/- 10 minutes of T_0 . This rainfall threshold is used to remove instances of very weak convection or possible rainfall measurement error, while the wind speed anomaly is inspired by Kruse *et al.* (2022) and verifies a more significant cold pool gust front strength compared with the background flow conditions (given our interest in quantifying cold pool impacts on wind turbines).
- There is no rainfall from T_0-30 to T_0-10 minutes to reduce environmental contamination by recent or nearby convection,
175 as well as to reduce false positive cases that could actually be related to cold fronts with along-frontal precipitation.

- θ_v continuously decreases by at least 1.5 K. This θ_v threshold is chosen to match the temperature decrease threshold of Kruse *et al.* (2022), with their study in the Netherlands being similarly situated in coastal flatlands. We have increased the threshold to -1.5 K from the -2 K used in Kirsch *et al.* (2021) due to WiValdi’s coastal location and greater environmental moisture, which would likely reduce the amount of evaporative cooling.
- 180 • A θ_v drop of at least 1.5 K occurs within 30 minutes of T_0 . This θ_v gradient threshold ensures a more robust cold pool passage, while minimizing occurrences of more-gradual cooling associated with phenomena outside the scope of this study (i.e., sea breezes, diurnal cycle, etc.). The 30-minute time constraint is similar to that of past work (20 minutes for Kirsch *et al.*, 2021 and Kruse *et al.*, 2022). For context, changing this time constraint to 20 minutes or 60 minutes would decrease or increase detected cases by one-third, respectively.
- 185 • Finally, we prescribe that θ_v must increase after reaching its minimum value and that this increase occurs within 60 minutes of T_0 . This aligns with known cold pool horizontal structure (Kirsch *et al.*, 2024) and further reduces false positives associated with cold frontal passages. The inclusion of this criterion only removes a few cases from our dataset, but visual inspection reveals that these removed cases resemble cold fronts (not shown).

Cold pool events are included in our dataset if they meet the above criteria. As we require rainfall to be detected at WiValdi
 190 for a cold pool to be counted, we exclude cold pool cases where the parent convective cell’s rainfall misses WiValdi but the cold pool periphery crosses over the wind park. We conservatively define the ‘pre-cold pool environment’ as the environmental conditions present at T_0 -30 minutes, with findings by Kirsch *et al.* (2021) and Kruse *et al.* (2022) indicating that near-surface environmental conditions do not significantly change until at least T_0 -15 minutes. The 1-minute averaged environmental conditions at T_0 -30 minutes from the MWR, lidar, and mast data provide a proxy for the background environment prior to each of
 195 the detected cold pool passages.

2.3 Convective cell tracking

While weather station and meteorological mast observations can and have been used to identify convective cold pools (e.g., Kirsch *et al.*, 2021; Hoeller *et al.*, 2024), additional radar measurements can be useful to (1) confirm the presence of a parent convective cell linked to the ground-based cold pool (Kruse *et al.*, 2022) and (2) provide comparison between radar-derived
 200 convection characteristics and near-surface cold pool characteristics. Therefore, to supplement the WiValdi observational network, we track convective cells associated with the detected cold pool cases using DWD radar composite datasets.

We utilize the radar reflectivity (WN) composite dataset from DWD, which has 1 km x 1 km horizontal resolution and 5-minute temporal resolution over Germany. This dataset is derived from 5-minute terrain-following scans of the German C-band radar network with a range resolution of 1 km and azimuth resolution of 1° (Wapler, 2021; Wilhelm *et al.*, 2023). We then
 205 employ the Tracking and Analysis of Thunderstorms (TATHU) toolset (Uba *et al.*, 2022; Sena *et al.*, 2024) to systematically detect and track convective systems within the WN dataset. With TATHU, convective elements, or objects, are identified using a chosen threshold from a given 2D field from which a corresponding bounded polygon is drawn. Given the polygon boundary at each time step and a user-provided polygon overlap area percentage, identified convective elements can be linked in time,

including whether storms undergo splitting or merging during their lifecycle. Convective element characteristics (weighted centroid position, shape, size) are provided at each time step and statistical quantities of the given 2D field related to each convective element can be obtained.

For this study, we define a convective cell as a contiguous area of at least 15 km^2 with a minimum radar reflectivity of 19 dBZ, with a 10% polygon overlap criterion used to connect convection snapshots in time. While the size threshold is identical to the DWD detection and nowcasting tool KONRAD, the reflectivity threshold of 19 dBZ is much lower than the 46 dBZ chosen by recent studies (Wapler, 2021; Wilhelm *et al.*, 2023). Goudenhoofdt and Delobbe (2013) proposed a minimum 40-dBZ threshold to identify convective precipitation over Belgium, suggesting that lower thresholds could lead to a higher potential for storms to be classified as splitting or merging due to closer proximity with nearby convection. However, to ensure identification of a precipitating convective cell close in time to the observed cold pool (which is detected without any convection-type rainfall classification), as well as to more fully capture a convective cell's lifecycle from early development to late decay, we employ this lower 19-dBZ reflectivity threshold for cell tracking.

3 Temporal Evolution of Cold Pool Characteristics

3.1 Near-surface

Using the detection criterion outlined in Section 2.2, we identify 120 convective cold pools impacting WiValdi from 26 November 2020 - 30 November 2024. Table 2 highlights the non-uniform distribution of cold pool events throughout the year, with generally more cases in the warmer months of May through October. However, the lower availability of 1-minute ground station observations in warmer months indicates a likely under-count of cold pool passages in total. The greater pre-event surface saturation deficit ($q_{sat} - q$) during May-October indicates a likelihood for greater evaporative cooling of rainfall during warmer months, though WiValdi generally has a lower saturation deficit during summer months than the 4.7 g kg^{-1} median saturation deficit found by Kirsch *et al.* (2021) during summer months farther inland near Hamburg. With the near-surface temperature perturbation previously found to have a relatively strong inverse relationship with pre-event saturation deficit (Kirsch *et al.*, 2021), we expected that the reduced saturation deficit at WiValdi would lead to weaker cold pools on average (in terms of surface temperature decrease) than those observed near Hamburg. Although this is somewhat borne out by the decreases in θ_v (relative to T_0-30) for the warmest months of July and August, we do not find a strong relationship between saturation deficit and cold pool temperature decreases for other months. Various factors could influence this finding of a weak relationship, including the lower variability of environmental conditions at WiValdi due to its coastal location, the convection types associated with the cold pools identified by our detection algorithm, the cold pool region sampled at WiValdi (e.g., the coldest part may not have passed over the site), and the lower data availability for the ground weather station during summer months.

Similar to the monthly θ_v variations, the median of the maximum rainrates during cold pool events tends to be larger in warmer months, indicating that more intense convective precipitation occurs in warmer months as would be expected. However, higher maximum rainrate does not uniformly correlate with a stronger cold pool (except perhaps for July), in agreement with

| | Cases | Data Availability | 2-m Pre – Event Environment [T_0-30] | | | 2-m environmental changes <i>during</i> Cold Pool Events | | |
|------------|-------|-------------------|--|-------------------------------------|------------------------|--|---------------------------------|---------------------------------|
| | | | Θ_v [°C] | $q_{sat} - q$ [g kg ⁻¹] | U [m s ⁻¹] | $\Delta\Theta_v$ [°C] | Rainrate [mm hr ⁻¹] | ΔU [m s ⁻¹] |
| Jan | 5 | 86% | 6.0 | 0.9 | 6.9 | -3.1 | 7.7 | 2.7 |
| Feb | 7 | 98% | 5.5 | 0.9 | 4.3 | -2.6 | 6.0 | 0.6 |
| Mar | 11 | 72% | 4.1 | 1.0 | 3.8 | -2.0 | 3.7 | 2.5 |
| Apr | 13 | 57% | 5.8 | 1.3 | 3.1 | -3.1 | 4.9 | 2.0 |
| May | 11 | 52% | 12.6 | 2.2 | 2.9 | -2.6 | 7.5 | 1.0 |
| Jun | 11 | 44% | 17.0 | 2.7 | 4.9 | -2.4 | 11.0 | 1.6 |
| Jul | 18 | 65% | 19.8 | 4.0 | 2.2 | -3.5 | 11.3 | 1.5 |
| Aug | 17 | 72% | 19.9 | 3.2 | 3.0 | -3.1 | 6.1 | 1.8 |
| Sep | 3 | 68% | 12.7 | 1.8 | 2.9 | -2.6 | 7.4 | 1.5 |
| Oct | 12 | 84% | 12.1 | 2.1 | 3.5 | -2.4 | 11.2 | 1.6 |
| Nov | 7 | 100% | 7.9 | 1.2 | 3.9 | -2.5 | 8.7 | 3.1 |
| Dec | 5 | 97% | 6.7 | 1.0 | 6.8 | -2.9 | 8.7 | 4.4 |

Table 2. Monthly climatology of detected cold pool cases, 1-minute ground station data availability, 2-m median pre-event environmental conditions (30 minutes *before* detected cold pool passage; e.g., T_0-30) in terms of θ_v (°C), saturation deficit ($q_{sat} - q$, g kg⁻¹), and total wind speed (m s⁻¹), and 2-m median environmental changes *during* cold pool events (relative to T_0-30) in terms of minimum θ_v (°C), maximum rainfall rate (mm hr⁻¹), and maximum total wind speed (m s⁻¹). The pre-event environment provides a proxy for the background environment. Gray shading indicates the warm season at WiValdi as shown by θ_v .

the weak relationship ($r = -0.38$) found by Kirsch *et al.* (2021). Past work over Germany has noted that accumulated rainfall, rather than maximum rainrate, has a stronger influence on the observed near-surface temperature drop (Kirsch *et al.*, 2024). Beyond the thermodynamic monthly climatology, we generally find higher background wind speeds in winter months, notably
245 December and January, in agreement with long-term wind climatologies over Europe (e.g., Molina *et al.*, 2021). Given this wind pattern and the positive daily wind anomaly criterion that we use in our detection methodology, it is not unexpected that the maximum near-surface wind speeds associated with the cold pool gust fronts tend to be larger during colder months. Nevertheless, there are still notable increases in 2-m wind speeds during warmer months on the order of 1-1.5 m s⁻¹.

As with the monthly variability of pre-event environments and cold pool events, there is a variety of parent convective cells
250 associated with the detected cold pools across all seasons, which are represented by the radar reflectivity snapshots in Figure 2 from the nearest radar times to their respective T_0 times. To better contextualize the monthly climatologies and these convection snapshots, we provide a brief case study for a cold pool that was detected on 15 June 2024 at 0854 UTC that is at the stronger end of the range of detected cold pool events. This cold pool occurred on a convectively-active day and was associated with a mesoscale convective system in northern Germany (Fig. 2c). Stratiform rainfall preceded the cold pool passage, and additional
255 cold pools were detected at WiValdi later that morning (not shown). As the gust front approached, there was an increase in wind speeds from 7 to 14 m s⁻¹ (Fig. 3a) alongside a wind direction shift from 195 to 235° (Fig. 3b) over the course of a few minutes. A significant increase in TKE dissipation rate ε (see Section 3.2) from T_0-30 minutes to T_0 highlights the greater turbulence strength associated with this gust front passage relative to the background flow (Fig. 3c). Immediately after the gust

front, there was a relative drop in θ_v of almost 3 K at the surface and 2.5 K at hub height over the course of 10-15 minutes, alongside intense rainfall up to 18 mm hr^{-1} which lasted until T_0+25 minutes (Fig. 3d). Wind speeds quickly subsided with the near-surface stabilization, while wind direction and ε more gradually shifted back towards their pre-event values. After 1 hour, the kinematic and thermodynamic near-surface atmosphere remained altered from the pre-event environment, though changes beyond about T_0+30 minutes are likely also impacted by subsequent convection occurring on this day.

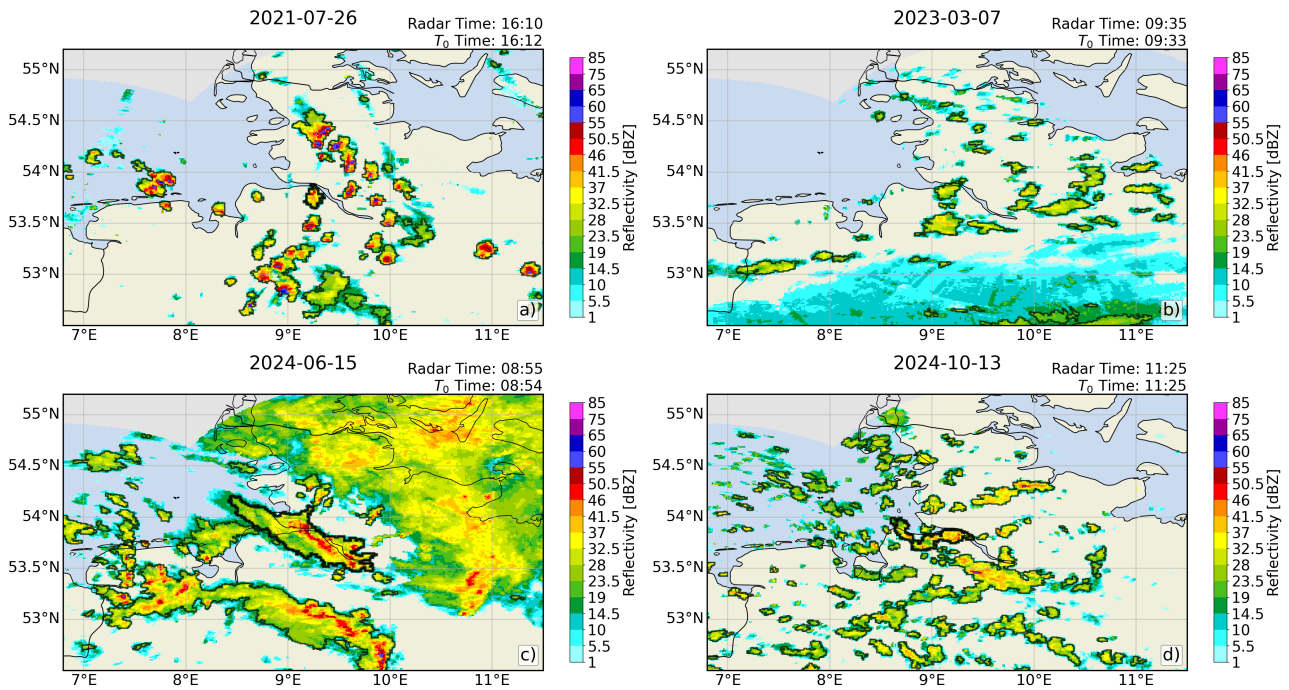


Figure 2. Snapshots of convection situations over northern Germany centered on WiValdi showing the radar reflectivity (dBZ, colors) for four parent convective cells representing the convection variability associated with the detected cold pool cases. Black contours denote polygon outlines for tracked cells. Bolded polygon outlines reflect when a tracked cell overlaps with WiValdi (a, c, d).

265

To gain an understanding of how the bulk near-surface atmospheric conditions change during the cold pool passages, we next examine median time series from the 2-m ground weather station observations (Fig. 4) for T_0-30 minutes to T_0+60 minutes. The median wind speed increases (dark blue) and the wind direction shifts more westerly (light blue) starting around T_0-15 minutes, with a more rapid increase in wind speed after T_0-5 minutes. This closely follows the temporal evolution of wind speed observed by Kirsch *et al.* (2021), with a relative increase of $1-1.5 \text{ m s}^{-1}$ by T_0+5 minutes being similar to their 2 m relative increase of 1.5 m s^{-1} . The median surface wind direction shifts towards westerly by up to 40° during the detected events. With T_0-30 minutes being a proxy for the pre-event environment, we find a median relative decrease in θ_v of 2.7 K (red) during the cold pool passages that occurs in the span of ~ 20 minutes, starting at T_0-5 minutes and reaching a minimum

270

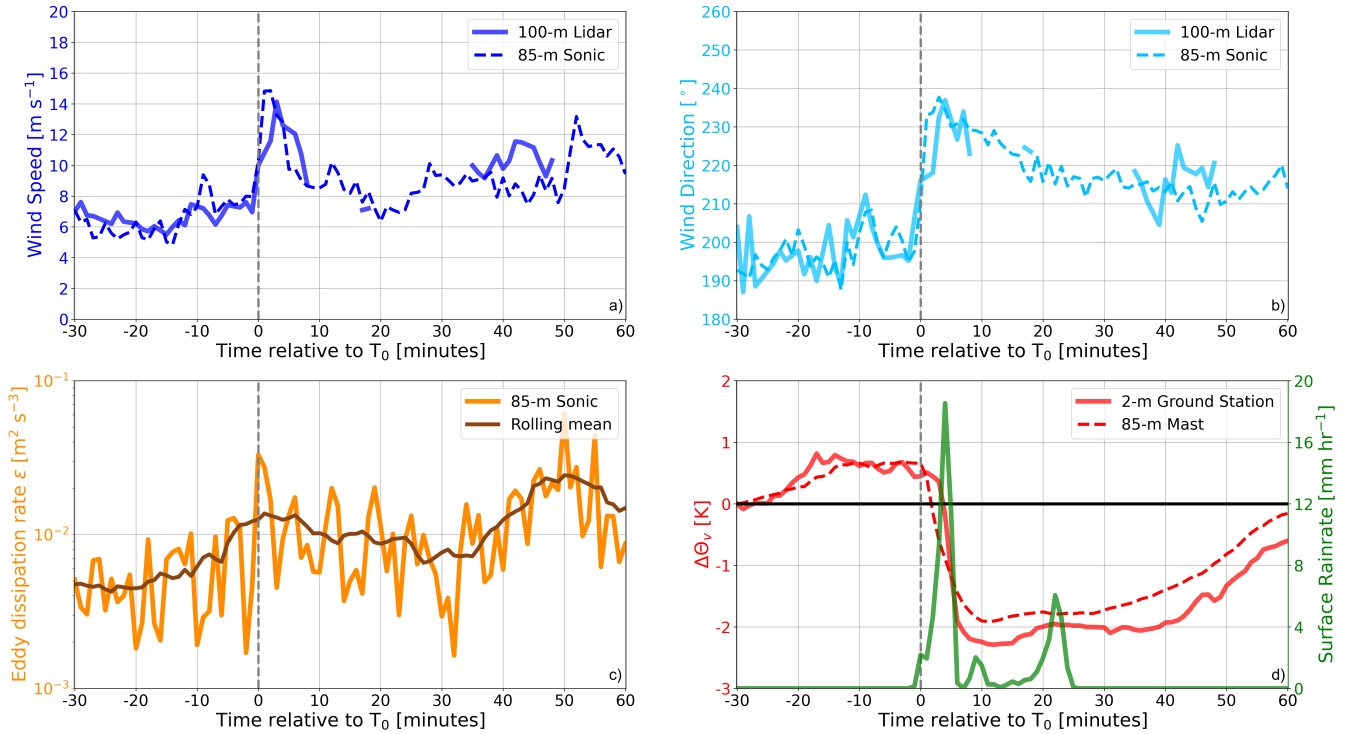


Figure 3. Case study on 15 June 2024 for $T_0 = 0854$ UTC. (a) wind speed (m s^{-1} ; dark blue), (b) wind direction ($^\circ$; light blue), (c) TKE dissipation rate ϵ ($\text{m}^2 \text{s}^{-3}$; orange), and (d) $\Delta\theta_v$ (K; red) and rainfall (mm hr^{-1} ; green). Solid colored lines indicate 100-m lidar (a-b), 85-m sonic (c), and 2-m ground station (d) data. Solid brown line in (c) is the 11-minute rolling mean ϵ . Dashed colored lines indicate 85-m sonic (a-b) and 85-m mast (c) observations. Lidar data with a signal-to-noise ratio below -25 and above 0 dB has been excluded from (a) and (b).

around T_0+15 to T_0+20 minutes. As in Kirsch *et al.* (2021), the θ_v drop onset slightly precedes T_0 by a few minutes due to our
 275 chosen detection thresholds. Shortly after this onset, measurable rainfall is observed which peaks near 2 mm hr^{-1} and lasts
 ~20 minutes. With a surface wind speed increase, wind direction shift, θ_v decrease, and measurable rainfall, the quintessential
 convective cold pool characteristics are observed at WiValdi.

After the cold pool gust front passage, which is strongly indicated by the rapid wind speed increase and θ_v drop onset at
 T_0-5 minutes, the near-surface wind speed gradually weakens to below the pre-event value and the near-surface wind direction
 280 gradually shifts back towards $\sim 230^\circ$ as the cold pool interior and parent convective cell pass by. The near-surface θ_v similarly
 recovers towards its pre-event state, though notably remains 1 K colder by T_0+60 minutes than at T_0-30 . This may suggest that
 cold pools are still propagating past WiValdi even 1 hour after the leading gust front, or at minimum that there is a lasting effect
 from the observed cold pools on the near-surface environment of at least 1 hour. Kruse *et al.* (2022) noted that temperature
 285 recovery typically occurred only after 2 hours for their cases in the Netherlands. So, while the kinematic changes accompanying
 the gust front are rapid (5-10 minutes) and would thus likely have an impact on turbine structural loads, the thermodynamic
 environment more gradually changes, with longer-lasting implications for turbine wakes and power generation.

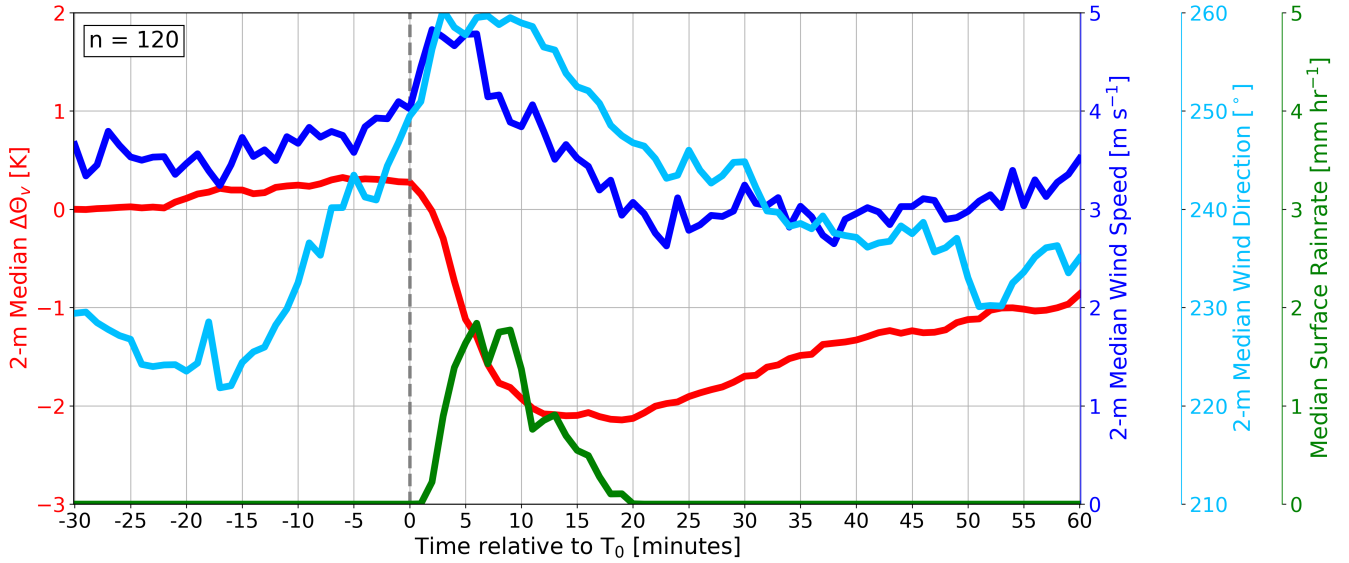


Figure 4. Median near-surface characteristics for the detected cold pool cases as measured by the 2-m ground station attached to the MWR relative to T_0 (dashed gray line), in terms of $\Delta\theta_v$ from T_0-30 minutes (K; red), wind speed (m s^{-1} ; dark blue), wind direction ($^\circ$; light blue), and rainfall (mm hr^{-1} ; green). Detected cold pool sample size is given in the upper left.

3.2 Hub-height

Moving above the surface to turbine hub-height, we want to quantify how much the kinematic and thermodynamic environment changes from the pre-event state. For wind speed and direction (Fig. 5a-b), we perform comparisons between 100 m
 290 lidar winds and an 85 m sonic on the inflow meteorological mast (west of T1), noting a decreased sample size of detected cold pool events from those observed by the ground station (Fig. 4). Both measurement systems similarly find a relative wind speed increase of 4 m s^{-1} on top of the background flow that peaks around T_0+5 minutes (Fig. 5a), with recovery to the pre-event wind speed typically by T_0+20 minutes. The 10th and 90th percentiles show a similar spread of wind speed changes, indicating that the 1-minute lidar scans are able to reasonably capture both the median and range of observed cold pool-associated
 295 hub-height wind speed variations. Of note, the timing of the gust front and recovery to the background flow as captured by the sonic tend to slightly precede that of the lidar by a couple minutes, which can largely be explained by the $\sim 1 \text{ km}$ instrument separation (with the more-westward sonic likely being impacted by cold pool passages before the lidar in most instances). Wind direction comparisons show a similar agreement between lidar and sonic (Fig. 5b). There is a peak wind direction change of $+15^\circ$ between T_0 and T_0+10 minutes which then gradually decreases, though the median relative wind direction change for
 300 both instruments does not recover to its pre-event value even after 1 hour. Though there is a sample size difference between sonic and lidar, the relative magnitude and spread of kinematic variations during cold pool passages at WiValdi are remarkably consistent between the *in-situ* and remote-sensing observations.

As past cold pool studies have noted an increase in turbulence associated with the gust front (Droegemeier and Wilhelmson, 1987; Lombardo *et al.*, 2014; Canepa *et al.*, 2020), and since turbulence strength correlates with stability regime and impacts turbine structural stress (e.g., Abkar and Porte-Agel, 2014; Englberger and Doernbrack, 2018), assessing short-term variations in turbulence is relevant for both convective cold pools and wind energy applications. The TKE dissipation rate ε is a metric for quantifying the turbulence strength, and is estimated herein every 1 minute using high-frequency (20 Hz) observations from the 85-m sonic on the inflow mast. Following Bodini *et al.* (2019), the theoretical turbulence model of Kolmogorov (Kolmogorov, 1941) is fit to the second-order structure function calculated from the sonic data using a range of time lags τ between 0.15 s and 1.05 s. Data inspection confirms that the sonic measurements within this time interval closely follow the Kolmogorov slope ($k = -5/3$), and hence lie within the inertial subrange of the turbulence energy spectrum. During the detected cold pool passages, there is a relative increase in median ε from the pre-event environment up to 10^{-2} around T_0 , indicating an increase in turbulence strength associated with the cold pool gust front (Fig. 5c). As turbulence tends to be greater during daytime hours and summertime months (Bodini *et al.*, 2019), which is also when most thunderstorms and thus convective cold pools would occur, the positive change in ε during the gust front would be in addition to this greater background turbulence pattern. After T_0 , there is a decrease in ε coinciding with the subsidence in wind speeds (Fig. 5a) and cooling of the near-surface atmosphere (Fig. 5d).

In contrast to the kinematic variations (Figs. 5a-b), the hub-height thermodynamic variations have noticeable disagreements in terms of θ_v between 1-minute inflow mast instrumentation and 1-minute MWR zenith retrievals at 85 m (Fig. 5d). While the median and 10th-90th percentile spread of relative θ_v changes follow a similar trend until the θ_v drop onset, a sizable proportion of MWR profiles remain warmer than the pre-event environment after T_0 in contrast to the in-situ observations. The 85-m MWR measurements are able to capture the first minutes of cooling after the gust front passage, but then the median values from the mast and MWR deviate from each other starting around T_0+5 minutes after a relative cooling to -0.5 K. The median mast observations indicate additional cooling to nearly -2 K by T_0+20 minutes, while the MWR profiles remain largely constant. This decrease in median mast θ_v at 85 m (Fig. 5d) shows a slightly weaker signal than near the surface (Fig. 4), which is consistent with previous studies (e.g., Kirsch *et al.*, 2021). As surface rainfall rates also typically increase within this time period from T_0+5 to T_0+20 minutes (Fig. 4), it is likely that raindrops on the MWR radome are interfering to some extent with the zenith retrievals for the measured frequencies in the microwave spectrum, particularly those in the water vapor absorption band. Foth *et al.* (2024) note that MWR retrieval algorithms generally decrease in accuracy for greater rainfall rates, with the zenith elevation angle having the largest positive brightness temperature biases (>3 K) across most measured frequencies compared with lower elevation angles. Additionally, as the thermodynamic vertical gradient between the surface and turbine hub-height also increases between T_0 and T_0+20 minutes (see Fig. 7), and since MWR zenith scans are less capable at capturing large vertical gradients, the MWR would be expected to have less accuracy during the time period of greatest cooling even if rainfall was not occurring. Both measurement systems show some recovery towards the pre-event state after T_0+20 minutes, though the MWR observations for most detected cold pool cases tend to have a persistent warm bias through T_0+60 minutes. Overall, the meteorological mast shows good agreement with the temporal evolution of θ_v given by the ground station (Fig. 4),

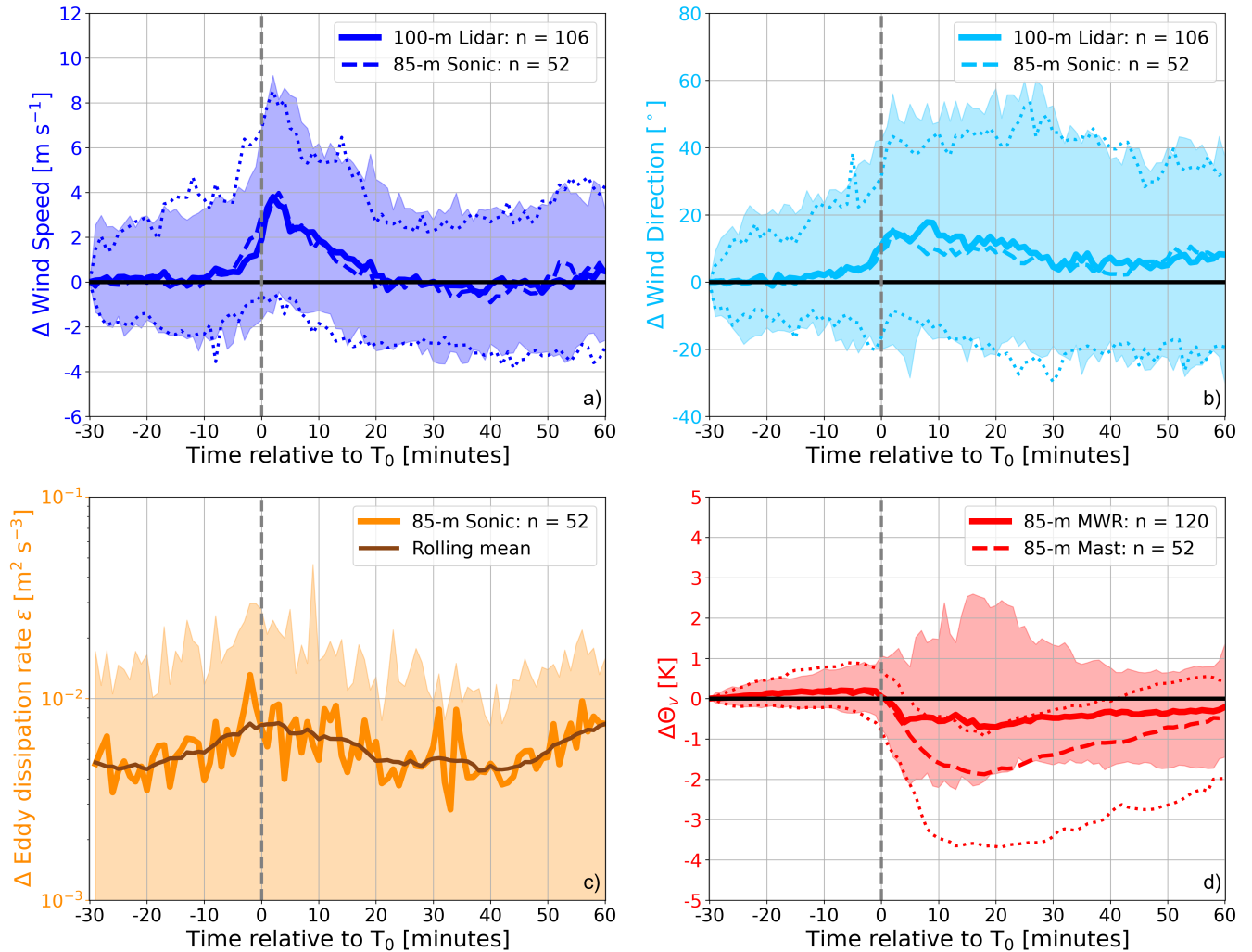


Figure 5. Hub-height variations relative to the pre-event environment (T_0 -30 minutes) and relative to T_0 (dashed gray line) for (a) wind speed (m s^{-1} ; dark blue), (b) wind direction ($^\circ$; light blue), (c) TKE dissipation rate ε ($\text{m}^2 \text{s}^{-3}$; orange), and (d) θ_v (K; red). Solid colored lines indicate 100-m lidar (a-b), (c) 85-m sonic ε , and (d) 85-m MWR, while dashed colored lines in (a-b, d) indicate 85-m in-situ inflow mast observations. Solid brown line in (c) is the 11-minute rolling mean ε , otherwise the darker solid and dashed colored lines indicate median values. Shading and thinner dashed colored lines indicate the 10th-90th percentile spread. Detected cold pool sample sizes given in the upper right for each instrument.

while the MWR profile measurements tend to underestimate the observed cooling within the cold pool interior. As such, we exclude the MWR profiles from our subsequent analyses.

4 Vertical Structure of Cold Pool Characteristics

340 As the wind speeds induced by cold pools often maximize above the surface within the height range of onshore wind turbines, we isolate the vertical structure associated with the peak gust front strength as shown in Figures 4 and 5 using vertical profiles up to 1 km height averaged from T_0 to T_0+5 minutes. Vertical profiles of relative wind speed from the lidar (Fig. 6a) highlight the increased winds associated with the cold pool gust front, with the largest relative increases occurring just above 100 m. The median wind speed shows a relative increase from the pre-cold pool environment up to about 800 m height, which
 345 provides a rough estimate for the median gust front depth at WiValdi. The relative wind direction profiles indicate a maximum shift of $+15^\circ$ (e.g., more westerly on average) also around 100-150 m height (Fig. 6b), with lower heights still typically exceeding $+10^\circ$. As the median relative wind direction vertical profile shows a positive wind direction shift up to 700 m height, this provides additional support for an approximate cold pool gust front depth of between 700-800 m. Notably, Kirsch *et al.* (2021) found an estimated median cold pool depth of 750 m near Hamburg using perturbation pressure extrapolation of mast data, which closely aligns with the zero-crossing height of the kinematic relative vertical profiles using the lidar at WiValdi.

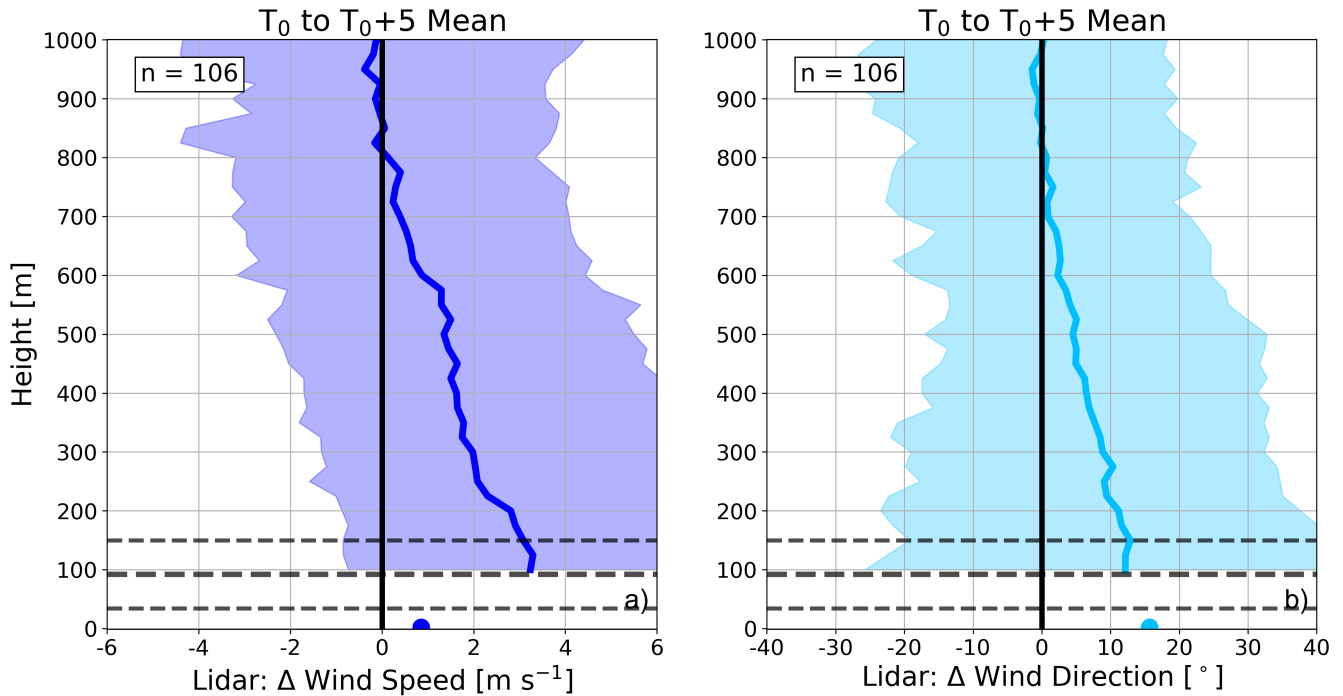


Figure 6. Mean vertical profiles over the given time periods relative to the pre-event environment (T_0-30 minutes) for (a) wind speed (m s^{-1} ; dark blue) and (b) wind direction ($^\circ$; light blue). Dots correspond to the median 2-m ground station observations averaged over the given time periods. Solid colored lines indicate the median conditions, while shading indicates the 10th-90th percentile spread. Horizontal dashed black lines indicate the turbine bottom (34 m), hub (92 m), and top (150 m). Detected cold pool sample size given in the upper left.

350

Focusing on the height region of the WiValdi turbines, we want to obtain a more detailed understanding of the vertical profile variations associated with the detected convective cold pools. There is a more limited sample size when all inflow mast instrumentation heights are available (Table 1), but the mast provides sufficient context for comparing with the remote-sensing vertical profiles. A typical gust front peaks in strength around the turbine hub-height at $+3 \text{ m s}^{-1}$ (Fig. 7a), exhibiting a nose shape within the turbine rotor layer (34-150 m; dashed black lines) as has been observed by past work on convective winds (Lombardo *et al.*, 2014; Gunter and Schroeder, 2015; Canepa *et al.*, 2020), with the vast majority of WiValdi cases showing increased wind speeds compared with the background flow. Indeed, both Kirsch *et al.* (2021) and Kruse *et al.* (2022) similarly observe positive wind speed perturbations associated with cold pool gust fronts maximizing around 100 m. While it appears that some gust fronts at WiValdi do not cause an increase in wind speed, this is actually a result of kinematic variations between T_0-30 and T_0 (see 10th percentile in Fig. 5a) which complicates the quantification of localized relative wind speed changes during the short time period of the gust front passage. Nevertheless, there is good agreement in the vertical shape and spread of wind speed above hub-height for the mast and lidar, further validating the remotely-sensed wind speeds. Notably, the mast data captures a greater wind speed change with height over the lower half of the rotor layer than the upper half. For the relative wind direction (Fig. 7b), a peak of $+15^\circ$ occurs close to the surface, in contrast to the wind speed peak that occurs near hub-height. The lidar relative wind direction changes between about 100-150 m are roughly comparable to the mast observations between these heights, qualitatively indicating that the lidar reasonably well captures the maximum wind direction changes accompanying the gust front. While there is a slightly greater wind direction change over the lower half of the rotor layer similar to the wind speed, the difference with the upper half is not quite as significant. The 'nose' in θ_v (Fig. 7c), with a lesser relative change at hub height compared to above and below, corresponds to the nose-like shape found in the wind speeds. Kirsch *et al.* (2021) find a similar 'nose' in θ_e at 110 m using mast observations at specific heights near Hamburg, however, this thermodynamic feature is not observed by Kruse *et al.* (2022) for cold pools over the Netherlands. We speculate that a θ_v 'nose' could perhaps be a manifestation of increased mixing in the gust front nose with the warmer background air ahead of the advancing cold pool, but we can not definitively identify the cause of this thermodynamic 'nose' feature, and so we leave this determination to future work.

By the time of maximum cold pool cooling (T_0+15 to T_0+20 minutes), the wind speeds have largely relaxed back towards the pre-event flow below hub height, though they remain increased by 1 m s^{-1} at turbine top (Fig. 7d). The wind direction adjustment is comparatively more subtle with some reduction in direction shift (Fig. 7e), but still being $5-10^\circ$ more westerly on average from T_0-30 minutes throughout the rotor layer, indicating that the wind direction typically takes longer to recover than the wind speed after cold pool gust front passages. Since the gust front time period (Fig. 7c), the relative θ_v shows greater cooling at all mast heights (Fig. 7f), being greatest near the surface at -2 to -2.5 K in agreement with the known vertical structure of the cold pool thermodynamical signal (e.g., Barnes and Garstang, 1982; Kirsch *et al.*, 2021). The 1-minute ground station observations seem to adequately capture the short-term environmental variations associated with the cold pools, with the possible exception of the initial near-surface θ_v drop (Fig. 7c), which is due to the inflow mast being impacted by the cold pool before the ground weather station (Fig. 1b). The observed rotor-layer cooling suggests stabilization throughout the profile within the cold pool interior, which will be explicitly quantified in the following section.

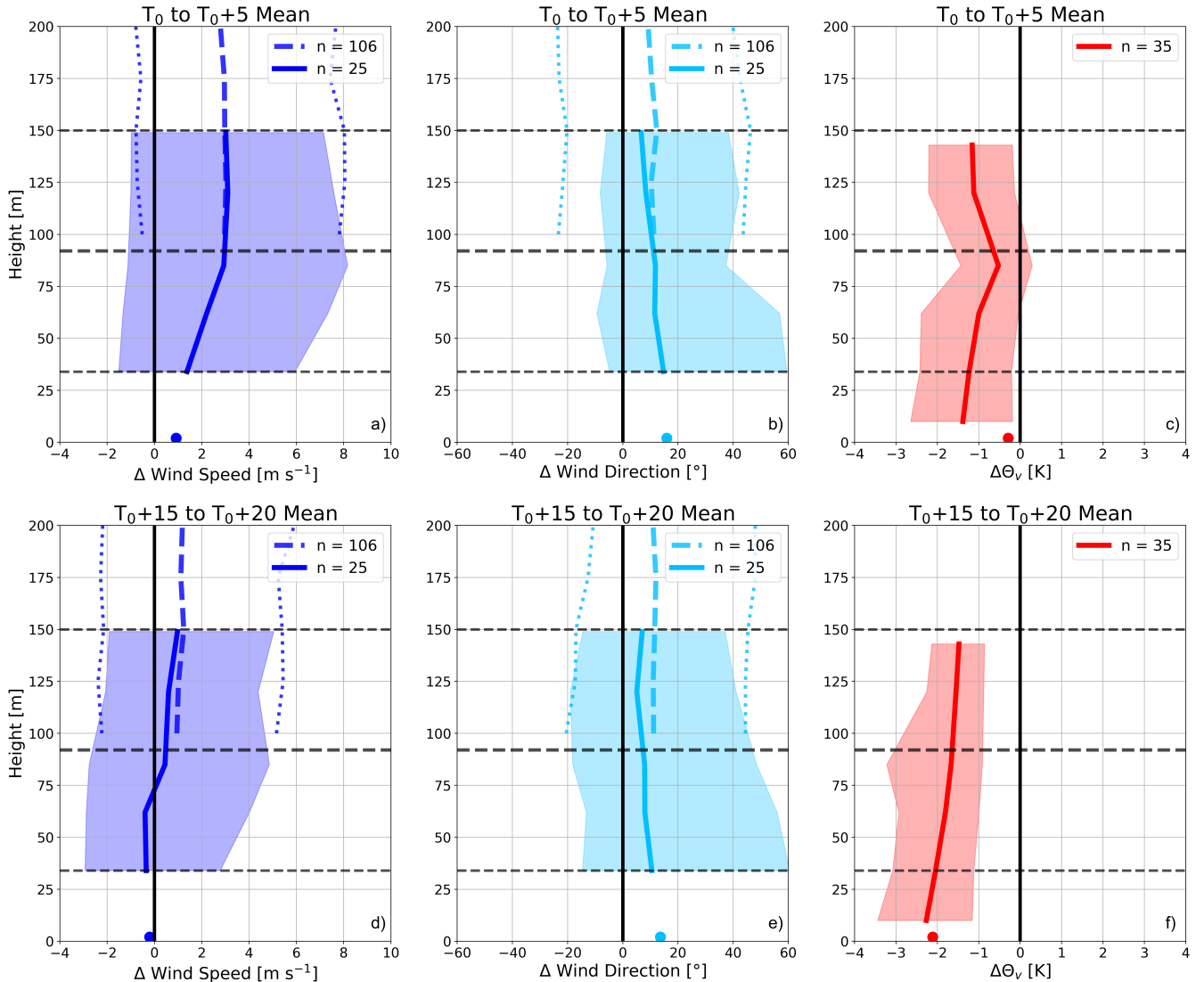


Figure 7. Mean vertical profiles within the turbine rotor layer over the given time periods for (a, d) wind speed (m s^{-1} ; dark blue), (b, e) wind direction ($^{\circ}$; light blue), and (c, f) θ_v (K; red) changes relative to T_0 -30 minutes using inflow mast (solid) and lidar (a-b, d-e; dashed) measurements. Horizontal dashed black lines indicate the turbine bottom (34 m), hub (92 m), and top (150 m). In-situ ground station measurements are shown as dots at 2 m. Median values shown in bold and thicker dashed colored lines, with 10th and 90th percentiles shown in shading and smaller dotted colored lines. Detected cold pool sample sizes per instrument given in the upper right.

5 Wind Turbine Rotor Layer

Now that we have examined how the temporal evolution and vertical structure of the background kinematic and thermodynamic environment is affected by convective cold pools at WiValdi, we next investigate variations in more-derived quantities

that affect power output and structural loads across the rotor layer associated with cold pool passages using inflow mast obser-
 390 vations. As indicated by the wind speed nose near hub height around T_0 to T_0+5 minutes (Fig. 7a), there is increased lower
 rotor-layer shear from the pre-event environment of 1.5 m s^{-1} (over a depth of 51 m) associated with the gust front alongside
 comparatively negligible changes in upper rotor-layer shear (Fig. 8a). Therefore, the total rotor-layer shear changes (over a
 depth of 115 m) induced by the cold pool gust front are almost exclusively encapsulated by shear changes below hub height.
 Upper rotor-layer shear increases more thereafter, peaking at 1 m s^{-1} (over a depth of 64 m) about 30 minutes after the gust
 395 front. The total rotor-layer shear remains increased by at least 1 m s^{-1} even 1 hour after T_0 , indicating that relative increases
 in shear-induced loads on the turbines would likely persist well after the cold pool leading edge. Similar to wind shear, the
 wind veer shifts the greatest around the time period of the gust front (Fig. 8b), noting that the relative wind veer is negative
 during WiValdi cold pool passages owing to greater wind direction changes closer to the surface (Fig. 7b). Veer across the
 lower part of the turbine rotor peaks at -6° around T_0 , with the total rotor-layer veer reaching -8° and the upper-layer veer
 400 peaking a few minutes later at -4° . Overall, the largest change in rotor-layer veer is associated with the cold pool leading edge,
 but a median shift in rotor-layer veer of -4° remains even after 1 hour. Given the 'nose' in relative θ_v around turbine hub height
 (Fig. 7c), there is a relative increase in static stability of 14 K km^{-1} over the lower rotor-layer and relative decrease in stability
 (greater instability) of 7 K km^{-1} over the upper rotor-layer (143-85 m) associated with the cold pool gust front (Fig. 8c). This
 asymmetric change in stability across the entire rotor layer continues until T_0+15 minutes, but it is unclear how the turbine
 405 wake would behave in this complex stability regime environment. Over the course of a thunderstorm passage, there is a general
 trend towards increasing stability compared with the pre-event environment as the near-surface cooling persists, remaining
 7 K km^{-1} more stable (0.8 K across the turbine rotor) after 1 hour. This longer-term stabilization throughout the rotor layer
 would tend to lengthen turbine wakes in the streamwise direction (Abkar and Porte-Agel, 2014), increasing the potential for
 downstream turbines to experience velocity deficits, decreased turbulence, and produce less power.

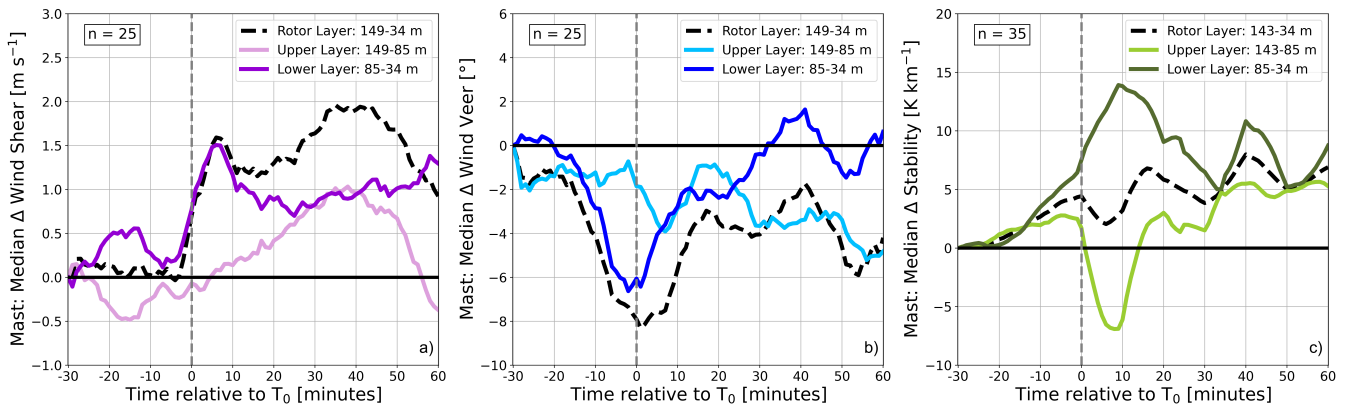


Figure 8. Median changes in inflow mast (a) wind shear (m s^{-1}), (b) wind veer ($^\circ$), and (c) static stability $\Delta\theta_v/\Delta z$ (K km^{-1}) relative to the pre-event environment (T_0-30 minutes) over the lower layer (85-34 m; darker lines), upper layer (149-85 m (a-b), 143-85m (c); lighter lines), and full rotor layer (149-34 m; dashed). Sample sizes given in the upper left.

410 Beyond shear and veer variations, we also seek to quantify the change in power generation that would be expected for a stand-alone turbine impacted by a cold pool. This has been modeled using a simple piecewise wind speed-power relationship (Wildmann *et al.*, 2022), wherein the cut-in, rated, and cut-out hub-height wind speeds are provided alongside the maximum turbine power output to obtain the 'estimated' power generation. Estimated power is taken to linearly increase between the cut-in and rated wind speeds (i.e., partial load range), and we do not consider impacts from turbine operational adjustments (e.g.,
415 pitching, yawing) on the power output. For the 4.2-MW WiValdi wind turbines, we have a 2.5 m s^{-1} cut-in, 13.1 m s^{-1} rated, and 25 m s^{-1} cut-out wind speed. With the 100-m lidar wind speeds being used as the hub-height wind input for this power estimate calculation, it is important to first determine where the background winds lie on the power curve to understand how much the subsequent cold pool wind speed perturbations may cause fluctuations in power generation. The 100-m pre-event environment typically has wind speeds of 9 m s^{-1} , with the 10-90th percentiles ranging from $4\text{-}15 \text{ m s}^{-1}$ (Fig. 9a). Therefore,
420 background hub-height winds are generally above the cut-in wind speed and within the partial load part of the power curve, indicating that most detected cold pool gust fronts would likely cause an increase in power output. When considering the climatological wind speeds at WiValdi (dashed lines, Fig. 9a), the pre-event flow is already elevated, suggesting that convective conditions before the cold pool time periods are already associated with a potential for greater than average power output. Lidar median wind speeds rise by 4 m s^{-1} in addition to the background flow during gust front passages (Fig. 5a), which reaches
425 the rated wind speed, and gust front amplitudes range from $3\text{-}6 \text{ m s}^{-1}$. As noted by Kelly *et al.* (2021), wind ramps starting below the rated wind speed and ending above the rated wind speed significantly contribute towards increased turbine structural loads, which closely aligns with the typical WiValdi cold pool. Using the above-mentioned power estimation and 100 m winds, we estimate a median increase in power output up to 50% around T_0 to T_0+5 minutes associated with the gust front (Fig. 9b). Estimated power increases can exceed 100% (for cases starting from weak background flow), and power generation remains
430 larger than the pre-event environment for about 30 minutes. We have a limited sample size of observed power output during the detected cold pools, but power observations from the westernmost WiValdi turbine (T1; Fig. 1b) during warmer months in 2024 broadly agree with having a significant peak associated with the gust front and increased power lasting about 30 minutes. After the gust front maximum, there is some indication of a relative reduction in observed wind power compared with the pre-event state, likely stemming from a relative decrease in hub-height wind speeds alongside the near-surface atmosphere stabilization.
435 As the observed power changes are complicated by continued turbine testing during the available time period and since this turbine was not always allowed to produce up to the rated power output, a larger observed power climatology in the future is needed to more reliably contextualize the estimated power generation. Nevertheless, we determine that noteworthy wind power increases would be expected for T1 due to the majority of cold pool gust fronts in the vicinity of WiValdi.

6 Summary and Conclusions

440 With the increasing amount of wind energy in Germany and remaining uncertainties regarding wind power prediction, it is crucial to better understand how particular atmospheric phenomena can impact wind turbines. Past literature has identified deep convection as one such phenomena linked to wind power prediction errors (Steiner *et al.*, 2017), with the associated convective

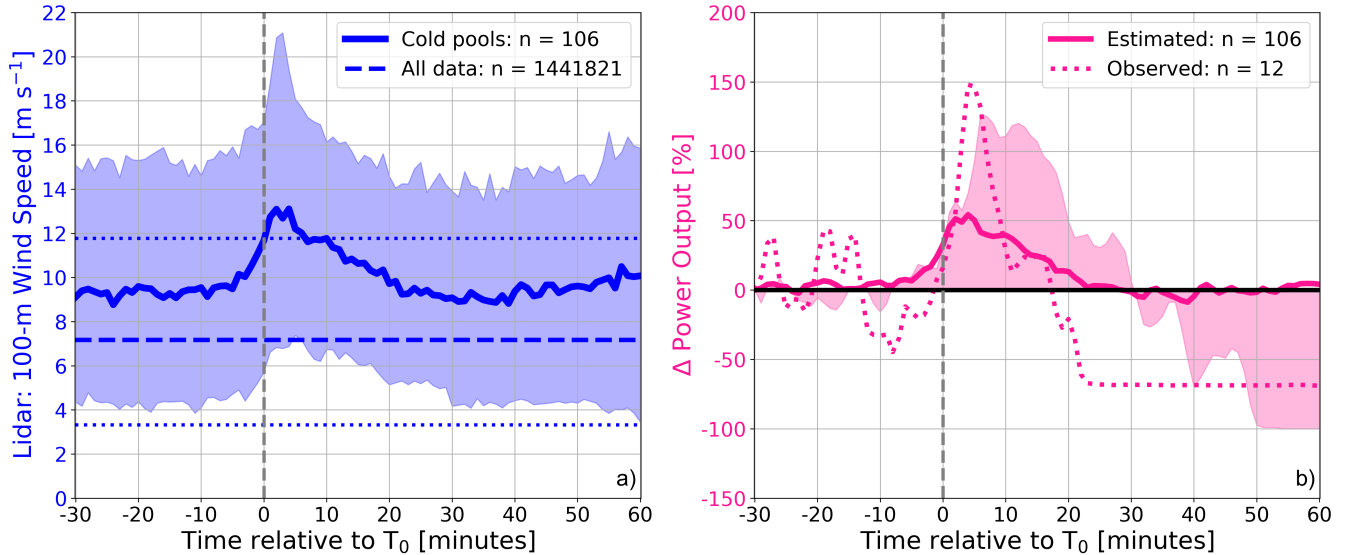


Figure 9. Time series relative to T_0 for (a) 100-m lidar wind speed (m s^{-1} ; dark blue) and (b) power output change relative to T_0 -30 minutes (%; pink). Solid lines indicate (a) median wind speeds around cold pool time periods and (b) median estimated power change. Thicker dashed lines indicate (a) 100-m climatological median wind speed and (b) observed median power change for the T1 turbine, with shading in (a, b) and thinner dashed lines in (a) indicating the 10-90th percentile spreads. Sample sizes given in the upper right.

outflow (i.e., cold pool) causing rapid changes in boundary-layer winds that are notoriously difficult for conventional forecasting models to characterize with sufficient spatial and temporal accuracy. To this end, we quantify the impact of convective cold pool passages on short-term environmental variations near two utility-scale onshore wind turbines in northern Germany at DLR’s WiValdi research wind park. We make extensive use of 1-minute meteorological mast and remote-sensing vertical profiles (Doppler wind lidar, MWR) in order to reliably capture the minute-scale ramp-up of thunderstorm winds (Lombardo *et al.*, 2014) and associated thermodynamic fluctuations. Cold pool events are identified from ground weather station data using thresholds for a continuous decrease in near-surface virtual potential temperature (θ_v), a positive daily wind anomaly, and measurable rainfall following from the methodologies of Kirsch *et al.* (2021) and Kruse *et al.* (2022). Of note, we define ‘ T_0 ’ as a proxy for the start of the cold pool passage similar to Kirsch *et al.* (2021), though the actual cold pool leading edge would precede this time by a few minutes due to the chosen threshold criterion. With the 120 detected cold pool cases across 4 years (November 2020 - November 2024), we primarily focus on kinematic and thermodynamic changes within the turbine rotor layer (34-150 m) associated with the cold pool leading edge (i.e., gust front) and the subsequent thermal stabilization within the cold pool interior.

A typical WiValdi convective cold pool follows the quintessential sequence of environmental changes: surface wind speeds increase and the wind direction shifts a few minutes before a drop in near-surface θ_v , which is then followed by rainfall 5-10 minutes later that peaks near 2 mm hr^{-1} . Of greater importance for wind energy, the median wind speeds relatively increase

by up to 4 m s^{-1} just above 100 m height compared with the pre-event flow (taken as T_0 -30 minutes) during the time period
460 from T_0 to T_0+5 minutes, with a relative increase in wind speeds for about 30 minutes. The hub-height wind direction shifts
more westerly on average than the background flow by $+15^\circ$, with full recovery to the background wind direction not reached
even after 1 hour. Turbulence strength, which we quantify using the dissipation rate of turbulent kinetic energy calculated from
high-frequency ultrasonic anemometer measurements, similarly shows a relative increase around the gust front time period.
After the kinematic variations associated with the passage of the cold pool gust front, the near-surface atmosphere cools for
465 20 minutes until reaching a minimum relative θ_v decrease of -2.7 K from its maximum value, with a relative decrease of -0.5
to -1 K still remaining after 1 hour. We determine that the gust front ramp-up starts from T_0-5 to T_0 minutes and peaks from T_0
to T_0+5 minutes, while the minimum θ_v (i.e., maximum cooling), which would be approximately the cold pool center (Kirsch
et al., 2024), is reached by T_0+15 to T_0+20 minutes. This yields a time from the cold pool leading edge to the cold pool center
on the order of 20-25 minutes. The peak wind speed and maximum cooling time periods are used for subsequent analyses to
470 isolate the largest environmental changes associated with the cold pool passages.

Using available vertical profiles from a Doppler wind lidar for 106 of the 120 cases, we estimate a median cold pool
depth of 700-800 m over which relative kinematic changes induced by the cold pool gust front are detectable. This is in good
agreement with a median cold pool depth of 750 m found by Kirsch *et al.* (2021) using pressure perturbation extrapolation
of meteorological mast data, and highlights that a typical cold pool depth would exceed the height of current onshore wind
475 turbines. As this lidar can not provide consistent temporal coverage below 100 m height due to the scanning pattern, we
leverage in-situ instrumentation on an inflow meteorological mast to provide greater vertical coverage within the turbine rotor
layer, though with a more-limited sample size. We find a 'nose shape' in increased wind speeds near hub height during the gust
front passages in line with past observational work focused on convective winds (Lombardo *et al.*, 2014; Gunter and Schroeder,
2015; Canepa *et al.*, 2020), and which is associated with a lesser relative decrease in θ_v at hub height compared to above and
480 below hub height. The relative wind direction and θ_v changes maximize near the surface, though a shift in direction of $+5-15^\circ$
during the gust front and cooling of $1.5-2 \text{ K}$ from T_0+15 to T_0+20 minutes is still observed on average throughout the rotor
layer. In terms of the bulk cold pool characteristics (strength, temporal evolution, vertical structure) related to kinematic and
thermodynamic variations, we are in broad agreement with other European cold pool studies (Kirsch *et al.*, 2021; Kruse *et al.*,
2022). However, the 'nose' in θ_v near hub height is one cold pool feature also found by Kirsch *et al.* (2021) that is not observed
485 by Kruse *et al.* (2022). As such, additional observational work is needed to determine if this aspect of the cold pool vertical
structure is commonly found, since its impact on wind turbine wakes in terms of static stability is crucial for assessing the net
impact of convective cold pools on wind power production in whole wind farms.

We extend beyond typical cold pool analyses by investigating fluctuations in shear, veer, and static stability, which are
important for wind power prediction and are more commonly studied in the wind energy community. The environmental
490 variations as the gust front impacts WiValdi produce rapid increases in relative wind shear of 1.5 m s^{-1} and negative relative
wind veer of 8° over the entire turbine rotor layer, with an increase in static stability of a few K km^{-1} . However, these
changes are not uniform across the turbine, but are rather asymmetric. The relative changes below turbine hub-height noticeably
exceed those above hub-height: upper-rotor-layer shear is negligible, with the relative wind veer and stability magnitudes being

twice as large below hub-height compared to above hub-height. Also, while there is an increase in stability below hub-height, there is a temporary decrease in stability above hub-height. With these vertical asymmetries, we would expect temporarily opposite fluctuations in static stability along with differential turbine structural loads across the rotor plane during cold pool gust front passages. Gradually increasing stabilization over the following hour across the whole rotor layer would have longer-lasting implications for turbine wake lengths, which can significantly affect downstream power output depending on wind farm configurations. Similarly, as wind direction more slowly shifts back towards the pre-event flow than wind speed, there would be longer-lasting effects on turbine yawing and structural loading from rotor-layer veer.

As the pre-event winds typically lie above the cut-in wind speed (2.5 m s^{-1}) and below the rated wind speed (13.1 m s^{-1}), we expected that cold pools would produce some wind power variations. To better quantify the potential power changes, we use the 100-m lidar wind speeds, a linear wind speed-power relationship within the partial load region of the power curve, and the operational settings of the WiValdi turbines. We estimate a median relative power increase of up to 50% associated with the cold pool gust front for the first WiValdi turbine impacted by the cold pools (e.g., T1), with a positive change in estimated power lasting 30 minutes. Although with just a handful of available power cases, the observed power variations qualitatively support a gust front peak and increased power occurring over approximately 0.5 hours. The median estimated percentage change in power due to the detected cold pool cases is noteworthy, however, the real-world significance of such a power change depends upon a number of factors beyond the scope of this study, including how many turbines are affected, whether the cold pool occurs during a power transition period (e.g., early evening), and whether cold pools affect whole wind parks. As such, the determination of the net impact of cold pools on observed wind power changes is left for future work. Greater investigation relating observed cold pool characteristics with parent convective cell characteristics is needed to reduce wind power forecasting uncertainties related to deep convection.

Throughout our analyses, we highlight the remarkable capabilities of a vertically-scanning Doppler wind lidar to capture both the temporal evolution and vertical structure of short-term wind speed and direction changes associated with convective cold pools in terms of both the median and 10th-90th percentile spread. Conversely, we note an underestimation of the hub-height θ_v variations by the 1-minute MWR zenith scans, particularly during periods of rainfall. Future studies should investigate whether rainfall corrections and/or different 1-minute MWR scanning patterns could remedy this limitation during convective cold pool passages. While we have a sufficient sample size of detected cold pools from the meteorological mast observations to support our conclusions regarding the kinematic and thermodynamic variations at WiValdi, additional mast measurements up to heights of 100-200 m over a larger number of locations would be beneficial to capturing the vertical structure of cold pools within the turbine rotor layer. A greater density of operational weather stations, in combination with more meteorological masts, would allow for more accurate quantification of cold pool sizes and thus how many wind turbines a given cold pool could impact. Given that our cold pool observations are from an onshore wind park, we take care not to generalize our findings to offshore wind farms. Future work should be mindful in applying the cold pool impacts described herein to offshore platforms or farther inland locations as the saturation deficit will likely cause differences in cold pool strength and vertical structure than we observe at our coastal location.

As this study deals with the intersection of convective cold pools and wind energy, we would like to suggest some possible additions to analysis done within each respective community from our understanding of past literature included in this work.

530 Cold pool studies should also quantify turbulence variables, shear, veer, and static stability (where possible) when analyzing the vertical structure of cold pools since these quantities are very beneficial for the wind energy community and wind energy applications. Conversely, wind ramp research should focus on both kinematic and *thermodynamic* changes occurring alongside wind ramps, as wind ramps linked to meteorological phenomena are often also associated with thermal variations, and since both aspects are important for assessing turbine structural loads, turbine wake characteristics, and wind power generation.

535 **7 Code availability**

Currently, the code is not publicly available.

8 Data availability

Currently, the data is not publicly available.

9 Author Contributions

540 All authors conceived of the paper idea. JT created the cold pool detection methodology. NW and JT performed the lidar and microwave radiometer data collection and processing. GK performed the radar data collection and analysis. JT performed all other observational data analyses, with constructive insights from GK and NW. The manuscript writing was primarily done by JT, with edits done by GK and NW.

10 Competing interests

545 The authors declare that they have no conflicts of interest.

11 Acknowledgements

We must particularly thank those that helped with the construction and implementation of the WiValdi research wind park, from where we obtained the majority of our data. We also acknowledge Martin Hagen for help with the microwave radiometer data collection and processing, as well as helpful comments on this manuscript. We are grateful to two anonymous reviewers for their thoughtful and thorough reviews of the original manuscript. This work used resources of the Deutsches Klimarechenzentrum (DKRZ) granted by its Scientific Steering Committee (WLA) under project ID bd1069.

550

12 Financial Support

This research was partially funded within the DFWind2 project (FKZ 0325936A) funded by the German Federal Ministry for Economic Affairs and Climate Action (BMWK) based on a resolution of the German Bundestag.

555 13 References

- Abkar, M., & Porté-Agel, F., 2014: Influence of atmospheric stability on wind-turbine wakes: a large-eddy simulation study. *Phys Fluids*, **27**(3):035,104. <https://doi.org/10.1063/1.4913695>.
- Barnes, G.M., & Garstang, M., 1982: Subcloud layer energetics of precipitating convection. *Mon. Wea. Rev.*, **110**, 102–117. [https://doi.org/10.1175/1520-0493\(1982\)110<0102:SLEOPC>2.0.CO;2](https://doi.org/10.1175/1520-0493(1982)110<0102:SLEOPC>2.0.CO;2).
- 560 Benjamin, T.B., 1968: Gravity currents and related phenomena. *Journal of Fluid Mechanics*, **31**, 209–248.
- BMWK, 2024: Time series for the development of renewable energy sources in Germany based on statistical data from the Working Group on Renewable Energy-Statistics (AGEE-Stat) (Status: September 2024). Report, 25 pp. https://www.bmwk.de/Redaktion_zur-entwicklung-der-erneuerbaren-energien-in-deutschland-1990-2023-en.pdf.
- Bodini, N., Lundquist, J. K., Krishnamurthy, R., Pekour, M., Berg, L. K., & Choukulkar, A., 2019: Spatial and temporal variability of turbulence dissipation rate in complex terrain. *Atmos. Chem. Phys.*, **19**, 4367–4382, <https://doi.org/10.5194/acp-19-4367-2019>.
- 565 Bouchard, R., & Romanic, D., 2023: Monte Carlo modeling of tornado hazard to wind turbines in Germany. *Nat Hazards*, **116**, 3899–3923. <https://doi.org/10.1007/s11069-023-05843-z>.
- Byers, H.R., & Braham, R.R., 1948: Thunderstorm Structure and Circulation. *J. Meteorol.*, **5**, 71–86. [https://doi.org/10.1175/1520-0469\(1948\)0052.0.CO;2](https://doi.org/10.1175/1520-0469(1948)0052.0.CO;2).
- 570 Canepa, F., Burlando, M., & Solari, G., 2020: Vertical profile characteristics of thunderstorm outflows. *J. Wind Eng. Ind. Aerod.*, **206**, 104332. <https://doi.org/10.1016/j.jweia.2020.104332>.
- Droegemeier, K., & Wilhelmson, R., 1987: Numerical simulation of thunderstorm outflow dynamics. Part I: Outflow sensitivity experiments and turbulence dynamics. *Journal of the Atmospheric Sciences*, **44**(8), 1180–1210. [https://doi.org/10.1175/1520-0469\(1987\)0442.0CO;2](https://doi.org/10.1175/1520-0469(1987)0442.0CO;2).
- 575 Englberger, A., & Doernbrack, A., (2018): Impact of the Diurnal Cycle of the Atmospheric Boundary Layer on Wind-Turbine Wakes: A Numerical Modelling Study. *Boundary-Layer Meteorol* **166**, 423–448.
- Foth, A., Lochmann, M., Saavedra Garfias, P.A., & Kalesse-Los, H., 2024: Determination of low-level temperature profiles from microwave radiometer observations during rain. *Atmos. Meas. Tech.*, **17**(24), 7169–7181. doi:10.5194/amt-17-7169-2024.
- 580 Fraunhofer ISE, 2024: German Net Power Generation in First Half of 2024: Record Generation of Green Power, Generation from Fossil Fuels Continues Decline. Accessed 3 July 2024. <https://www.ise.fraunhofer.de/en/press-media/press-releases/2024/german-net-power-generation-in-first-half-2024-record-generation-of-green-power-generation-from-fossil-fuels-continues-decline.html>.

- 585 Gallego-Castillo, C., Cuerva-Tejero, A., & Lopez-Garcia, O., 2015: A review on the recent history of wind power ramp forecasting. *Renew Sustain Energy Rev.*, **52**:1148-1157. <https://doi.org/10.1016/j.rser.2015.07.154>.
- Goff, R.C., 1976: Vertical structure of thunderstorm outflows. *Monthly Weather Review*, **104(11)**, 1429–1440.
- Goudenhoofdt, E., & Delobbe, L., 2013: Statistical Characteristics of Convective Storms in Belgium Derived from Volumetric Weather Radar Observations. *J. Appl. Meteor. Climatol.*, **52**, 918–934, <https://doi.org/10.1175/JAMC-D-12-079.1>.
- 590 Gunter, W.S., & Schroeder, J.L., 2015: High-resolution full-scale measurements of thunderstorm outflow winds. *J. Wind Eng. Ind. Aerod.*, **138**, 13–26. <https://doi.org/10.1016/j.jweia.2014.12.005>.
- Hansen, K.S., Barthelmie, R.J., Jensen, L.E., & Sommer, A., 2012: The impact of turbulence intensity and atmospheric stability on power deficits due to wind turbine wakes at Horns Rev wind farm. *Wind Energy*, **15(1)**:183–196.
- Hoeller, J., Fiévet, R., & Haerter, J.O., 2024: Detecting cold pool family trees in convection resolving simulations. *Journal of*
- 595 *Advances in Modeling Earth Systems*, **16**, e2023MS003682. <https://doi.org/10.1029/2023MS003682>.
- Iungo, G.V., & Porté-Agel, F., 2014: Volumetric lidar scanning of wind turbine wakes under convective and neutral atmospheric stability regimes. *J Atmos Ocean Technol*, **31(10)**:2035–2048. <https://doi.org/10.1175/JTECH-D-13-00252.1>.
- Kelly, M., Andersen, S.J., Hannesdóttir, Á., 2021: Statistical impact of wind-speed ramp events on turbines, via observations and coupled fluid-dynamic and aeroelastic simulations. *Wind Energy Sci.*, **6(5)**, 1227–1245.
- 600 Kirsch, B., Ament, F., & Hohenegger, C., 2021: Convective cold pools in long-term boundary layer mast observations. *Monthly Weather Review*, **149**, 811–820.
- Kirsch, B., Hohenegger, C., & Ament, F., 2024: Morphology and growth of convective cold pools observed by a dense station network in Germany. *Quarterly Journal of the Royal Meteorological Society*, **150(759)**, 857–876. <https://doi.org/10.1002/qj.4626>.
- Kolmogorov, A.N., (1941): Dissipation of energy in locally isotropic turbulence. *Dokl. Akad. Nauk SSSR*, **32**, 16–18.
- 605 Kropfli, R.A., 1986: Single Doppler Radar Measurements of Turbulence Profiles in the Convective Boundary Layer. *J. Atmos. Oceanic Technol.*, **3**, 305-314. [https://doi.org/10.1175/1520-0426\(1986\)003<0305:SDRMOT>2.0.CO;2](https://doi.org/10.1175/1520-0426(1986)003<0305:SDRMOT>2.0.CO;2).
- Kruse, I.L., Haerter, J.O., & Meyer, B., 2022: Cold pools over the Netherlands: a statistical study from tower and radar observations. *Quarterly Journal of the Royal Meteorological Society*, **148**, 711–726.
- Larsén, X.G., Ott, S., Badger, J., Hahmann, A.H., & Mann, J., 2012: Recipes for correcting the impact of effective mesoscale
- 610 resolution on the estimation of extreme winds. *J. Appl. Meteorology Climatol.*, **51**, 521–533. [doi:10.1175/JAMC-D-11-090.1](https://doi.org/10.1175/JAMC-D-11-090.1).
- Lee, J.C.Y., & Fields, M.J., 2021: An Overview of Wind Energy Production Prediction Bias, Losses, and Uncertainties. *Wind Energy Sci.*, **6**, 311–365. <https://doi.org/10.5194/wes-6-311-2021>.
- Lochmann, M., Kalesse-Los, H., Schäfer, M., Heinrich, I., & Leinweber, R., 2023: Analyzing wind power ramp events and
- 615 improving very short-term wind power predictions by including wind speed observations. *Wind Energy*, **26(6)**:573-588. [doi:10.1002/we.281](https://doi.org/10.1002/we.281).
- Lombardo, F.T., Smith, D.A., Schroeder, J.L., & Mehta, K.C., 2014: Thunderstorm characteristics of importance to wind engineering. *J. Wind Eng. Ind. Aerod.*, **125**, 121–132. <https://doi.org/10.1016/j.jweia.2013.12.004>.

- Molina, M.O., Gutiérrez, C., & Sánchez, E., 2021: Comparison of ERA5 surface wind speed climatologies over Europe with
620 observations from the Hadisd dataset. *Int J Climatol*, **1**:1–15. <https://doi.org/10.1002/joc.7103>.
- Rose, T., Crewell, S., Löhnert, U., & Simmer, C., 2005: A network suitable microwave radiometer for operational monitoring
of the cloudy atmosphere. *Atmos. Res.*, **75**, 183–200, <https://doi.org/10.1016/j.atmosres.2004.12.005>.
- Sena, C.A.P., Negri, R.G., Gava, M.L.L.M., 2024: GOES ABI-derived hailstorm polygons and tracking dataset for Brazil. *Data
in Brief*, **55**, 110736, ISSN 2352-3409. <https://doi.org/10.1016/j.dib.2024.110736>.
- 625 Steiner, A., Köhler, C., Metzinger, I., et al. 2017: Critical weather situations for renewable energies – Part A: cyclone detection
for wind power. *Renew Energy*, **101**:41-50. doi:10.1016/j.renene.2016.08.013.
- Stull, R.B., 1988: An Introduction to Boundary Layer Meteorology. Atmospheric and Oceanographic Sciences Library, Vol.
13, Kluwer Academic, 670 pp.
- de Szoeke, S.P., Skyllingstad, E.D., Zuidema, P., & Chandra, A.S., 2017: Cold pools and their influence on the tropical marine
630 boundary layer. *Journal of the Atmospheric Sciences*, **74**, 1149–1168.
- Uba, D.M., Negri, R.G., Enoré, D.P.; Costa, I.C., Jorge, A.A.S., 2022: TATHU - Software para rastreio e análise do ciclo de
vida de sistemas convectivos. São José dos Campos: INPE. 39 p. IBI: <8JMKD3MGP3W34T/47AF772>. (sid.inpe.br/mtc-
m21d/2022/07.20.15.45-NTC). <<http://urlib.net/ibi/8JMKD3MGP3W34T/47AF772>>.
- Valldecabres, L., von Bremen, L., & Kühn, M., 2020: Minute-scale detection and probabilistic prediction of offshore wind
635 turbine power ramps using dual-Doppler radar. *Wind Energy*, **23**, 2202–2224. <http://dx.doi.org/10.1002/we.2553>.
- Vincent, C.L., Pinson, P., & Giebela, G., 2011: Wind fluctuations over the north sea. *Int J Climatol.*, **31(11)**:1584-1595.
- Wakimoto, R.M., 1982: The life cycle of thunderstorm gust fronts as viewed with Doppler radar and rawinsonde data. *Monthly
Weather Review*, **110**, 1060–1082.
- Wapler, K., 2021: Mesocyclonic and non-mesocyclonic convective storms in Germany: storm characteristics and life-cycle.
640 *Atmospheric Research*, **248**, 105186.
- Wildmann N, et al. , 2018; Coplanar lidar measurement of a single wind energy converter wake in distinct atmospheric stability
regimes at the Perdigão 2017 experiment. *J. Phys.: Conf. Ser.*, **1037**, 052006, DOI 10.1088/1742-6596/1037/5/052006.
- Wildmann, N., Päschke, E., Roiger, A., & Mallaun, C., 2020: Towards improved turbulence estimation with Doppler wind
lidar velocity-azimuth display (VAD) scans. *Atmospheric Measurement Techniques*, **13(8)**, 4141-4158. doi: 10.5194/amt-
645 13-4141-2020.
- Wildmann, N., Hagen, M., & Gerz, T., 2022: Enhanced resource assessment and atmospheric monitoring of the research wind
farm WiValdi. *Journal of Physics Conference Series*, **2265**, 022029. <https://doi.org/10.1088/1742-6596/2265/2/022029>.
- Wildmann, N., Thayer, J.D., Detring, C., & Päschke, E., 2024: Gust-detection from velocity azimuth display Doppler wind
lidar profiling at the WiValdi research park. *Journal of Physics: Conference Series*, **2767(2024)**, 092076. doi:10.1088/1742-
650 6596/2767/9/092076.
- Wilhelm, J., Wapler, K., Blahak, U., Pothast, R. & Kunz, M., 2023: Statistical relevance of meteorological ambient conditions
and cell attributes for nowcasting the life cycle of convective storms. *Quarterly Journal of the Royal Meteorological Society*,
149(755), 2252–2280. Available from: <https://doi.org/10.1002/qj.4505>.

- Würth, I., Valdecabres, L., Simon, E., et al. 2019: Minute-scale forecasting of wind power—results from the Collaborative
655 Workshop of IEA Wind Task 32 and 36. *Energies*, **12(4)**:712. doi:10.3390/en12040712.
- Zhang, W., Markfort, C.D., & Porté-Agel, F., 2013: Wind-turbine wakes in a convective boundary layer: a wind tunnel study. *Boundary-Layer Meteorol*, **146(2)**:161–179. <https://doi.org/10.1007/s10546-012-9751-4>.